



OPEN Effect of synthesis methods, biocompatibility and photoluminescence of scheelite type sodium lanthanide double tungstates

Mahendra B. Choudhary¹, Delna Johnson², Deep Kumar Das³, Vijay Thiruvengadam⁴, Janardan Kundu³ & Venkatesha R. Hathwar¹✉

The scheelite type sodium lanthanide double tungstates $\text{NaRE}(\text{WO}_4)_2$ ($\text{RE} = \text{Sm}^{3+}$, Ho^{3+} and Pr^{3+}) were synthesized by three different synthesis methods, namely solid-state reaction, hydrothermal method and solvothermal method using ethylene glycol. The synthesized samples were characterized by X-ray diffraction (XRD), scanning electron microscopy, UV-DRS and photoluminescence spectroscopy. The phase pure sample preparations with the Scheelite-like crystal structure in $I4_1/a$ space group were established by XRD. Among the three synthesis methods, the broader XRD peaks were noticed for the solvothermal samples and resulting in crystallite sizes of $\sim 11\text{--}28$ nm. The SEM micrographs supported the XRD results and the agglomeration of particles with similar morphology was confirmed for all synthesis methods. The smallest particle size was obtained in the solvothermal method with average particle size distributions of $\sim 100\text{--}140$ nm. Indeed, the synthesis methods and particle size played a crucial role in the photoluminescence (PL) emission spectra. The PL emission intensity was very low for as-synthesized solvothermal samples where the particle size was considerably smaller compared to the other two methods. However, the calcination of solvothermal samples at different temperatures has improved their PL emission such that the emission intensity gradually increased with increasing the calcination temperature. Simultaneously, the SEM confirmed that the particle size remained the same till the calcination temperature of 600°C . The microbial cell viability and cytotoxicity experiments were performed on the solvothermal samples using *E. coli*, *S. aureus* and HeLa cells, respectively. The biological studies demonstrated the biocompatibility of synthesized samples. The biocompatibility and smaller particle size in the solvothermal method could be useful in developing improved phosphors for cell imaging and theranostic applications.

Keywords Double tungstate, Solvothermal, Particle size, Biocompatible, Photoluminescence

Alkaline rare-earth double tungstates with a general formula $\text{ARE}(\text{WO}_4)_2$, where A = monovalent alkali cation and RE = rare earth ion, have attracted considerable attention due to their attractive photoluminescence (PL) properties, high stability and biocompatibility¹. They display distinctive photoluminescent properties depending on the chemical composition, purity of samples, surface morphology, stability and particle size^{2–4}. The double tungstates are extensively explored as solid-state lighting phosphors^{5–7}, solid-state lasers^{8,9}, optical waveguide¹⁰, fluorescent bioprobes¹¹ and temperature sensors^{12,13}. Many attempted to achieve the particle size distribution during the synthesis and their effects on PL properties of rare-earth doped materials in the literature^{14,15}. Recently, lanthanide-doped tungstates have played a significant role in solid-state lighting applications and biophotonics¹⁶. The intense tunable luminescence emissions and nontoxicity were found to be useful in theranostic applications¹⁵. Yang et al. investigated the biocompatibility of $\text{NaLa}(\text{MoO}_4)_2:\text{Eu}^{3+}/\text{Tb}^{3+}$ on ARPE-

¹School of Physical and Applied Sciences, Goa University, Taleigao Plateau, Goa 403206, India. ²Department of Chemistry, Indian Institute of Technology Gandhinagar, Palaj, Gujarat 382355, India. ³Indian Institute of Science Education and Research (IISER) Tirupati, Tirupati, Andhra Pradesh 517507, India. ⁴Department of Biological Sciences and Engineering, Indian Institute of Technology Gandhinagar, Palaj, Gujarat 382355, India. ✉email: vhathwar@unigoa.ac.in

19 cells for in-vitro applications¹⁷. Further, NaLa(WO₄)₂:Eu³⁺ and NaLa(WO₄)₂:Eu³⁺/Tb³⁺ were explored to study the influence of sensitizer and activator concentration on the luminescence intensity^{18–20}. The effect of particle size of NaEu(WO₄)₂ was examined for the red emission properties and biocompatibility studies¹⁵. Indeed, NaGd(WO₄)₂:Pr³⁺, KLa(WO₄)₂:Eu³⁺, KGd_(1-x)Pr_x(WO₄)₂ and NaGd_(1-x)Eu_x(WO₄)₂ were used as novel red-emitting phosphors^{21–23}. Further, some of RE substituted double tungstates such as NaY(WO₄)₂:Sm³⁺²⁴, NaGd(WO₄)₂:Sm³⁺²⁵, NaGd(WO₄)₂:Ho³⁺²⁶, NaGd(WO₄)₂:Pr³⁺²⁷, NaGd(WO₄)₂:Eu³⁺²⁸, NaGd(WO₄)₂:Tb³⁺²⁹, NaY(WO₄)₂:Dy³⁺³⁰, have shown considerable improvement in the PL emission lifetime ranging from ms to μs and could be useful phosphors. The NaIn(WO₄)₂:Dy³⁺ phosphors demonstrated superior white light emission and could be encouraging for white light-emitting diodes³¹. The KYb(MoO₄)₂:Er³⁺ phosphor has demonstrated an excellent temperature sensing performance and has potential use as a temperature sensor³². Further, NaGd(MoO₄)₂:Dy³⁺/Eu³⁺ and NaGd(WO₄)₂:Dy³⁺/Eu³⁺ have been demonstrated as improved photocatalysts for the photodegradation of antibiotic drug, nitrofurantoin³³. The solid solution of Na(Gd_xLa_{1-x})(MoO₄)₂:Yb³⁺/Er³⁺ has shown simultaneously enhanced photothermal conversion efficiency and PL properties³⁴.

Previously, NaRE(WO₄)₂ (RE = Sm³⁺, Ho³⁺ and Pr³⁺) were synthesized by solid-state reactions at 800 °C for 10 h and XRD results indicated the presence of starting compounds, Na₂CO₃, WO₃ and Re₂O₃ as impurity phases during the synthesis³⁵. Further, there was no efforts to control the particle size of NaRE(WO₄)₂ (RE = Sm³⁺, Ho³⁺ and Pr³⁺) which is detrimental for the biocompatibility and anti-cancer studies. Additionally, the space group of NaPr(WO₄)₂ was determined as P2/n which seems to be controversial as the family of NaRE(WO₄)₂ compounds crystallize in the I4₁/a space group⁴. To resolve the above ambiguities, we have synthesized, NaRE(WO₄)₂ (RE = Sm³⁺, Ho³⁺ and Pr³⁺) by three different methods, namely solid-state reactions, hydrothermal method and solvothermal method where ethylene glycol (EG) was used as solvent. The phase pure samples with smaller particle size were obtained. The effect of the synthesis method on the particle size distribution, biocompatibility and PL properties are systematically investigated.

Experimental section

Materials

Na₂CO₃ (99.9%), WO₃ (99.9%), RE₂O₃ (99.9%) (RE = Sm³⁺, Ho³⁺ and Pr³⁺), Na₂WO₄·2H₂O (99.9%), Sm(NO₃)₃·6H₂O (99.9%), Ho(NO₃)₃·5H₂O (99.9%) and Pr(NO₃)₃·H₂O (99.9%) were used as starting materials to prepare NaRE(WO₄)₂ (RE = Sm³⁺, Ho³⁺ and Pr³⁺). Milli-Q water and EG were utilized as solvents. HNO₃ and NaOH solutions were used to manage the pH of the solution. All the materials were procured from Alfa Aesar and Sigma-Aldrich of analytical grade and used as such without further purification. MTT (3-(4,5-dimethylthiazol-2-yl)-2,5-diphenyltetrazolium bromide), Dulbecco's modified Eagle's medium (DMEM), penicillin, streptomycin, phosphate-buffered saline (PBS) and Fetal bovine serum (FBS) were used in pure form for the MTT assay. The human cervical cancer cell line, HeLa cells used for the cytotoxicity experiments were received from NCCS Pune, India. The microbial cytotoxicity studies were performed on bacterial strains *Escherichia coli* (*E. coli*) (ATCC 25922) and *Staphylococcus aureus* (*S. aureus*) (ATCC-25923) acquired from the Microbial Type Culture Collection (MTCC), Chandigarh.

Synthesis

Samples were synthesized by solid-state reaction method, hydrothermal method and solvothermal method.

Solid state reaction method

1 mmol of Na₂CO₃, 4 mmol of WO₃ and 1 mmol of RE₂O₃ (RE = Sm³⁺, Ho³⁺ and Pr³⁺) were weighed and thoroughly mixed in agate mortar by grinding for 30 min. Then finely ground mixture was transferred to an alumina crucible and annealed at 800 °C for 12 h. After cooling the furnace to room temperature, the reacted mixture was grounded and NaRE(WO₄)₂ (RE = Sm³⁺, Ho³⁺ and Pr³⁺) were obtained. The pure single-phase samples, NaSm(WO₄)₂ (**S1**), NaHo(WO₄)₂ (**S2**) and NaPr(WO₄)₂ (**S3**) were synthesized by the solid state reaction method.

Hydrothermal method

1 mmol of RE(NO₃)₃·xH₂O (RE = Sm³⁺, Ho³⁺ and Pr³⁺) (solution-A) and 2 mmol of Na₂WO₄·2H₂O (solution-B) were separately dissolved in 10 mL milli-Q water and stirred continuously. Afterwards, solution-A was mixed with solution-B in drop wise and simultaneously stirred for 30 min at room temperature. The white suspension was further diluted to 40 mL and the pH was maintained to be neutral using 0.1 mM NaOH and HNO₃. The resultant product is later transferred into a 100 mL Teflon-lined autoclave, sealed and heated at 200 °C for 24 h. After cooling the autoclave to room temperature, the resulting precipitate was collected by centrifugation. The white powder of NaSm(WO₄)₂ (**H1**) and NaHo(WO₄)₂ (**H2**) and light green powder of NaPr(WO₄)₂ (**H3**) were obtained after washing with milli-Q water and dried at 90 °C for 4 h.

Solvothermal method

The procedure was similar to the hydrothermal method, where water was replaced with EG as a solvent. Light greyish colour powder of NaSm(WO₄)₂ (**EG1**) and NaHo(WO₄)₂ (**EG2**) and light green powder of NaPr(WO₄)₂ (**EG3**) were obtained. In the case of **EG2**, 12 ml of milli-Q water was mixed with the solution to enhance the solubility of Ho(NO₃)₃·xH₂O in EG.

Characterizations

The sample purity and crystalline nature of samples were examined by XRD measurements performed at room temperature using monochromatic Cu-K_α radiation on a Rigaku Smartlab SE diffractometer operating at 40 kV and 50 mA in the 2θ range from 10° to 80° with step size of 0.02° and scan rate of 2°/min. Morphology,

particle size distribution and energy dispersive spectroscopy (EDS) spectrum were obtained in a Carl Zeiss, Evo 18 scanning electron microscopy (SEM). The diffuse reflectance spectra (UV-DRS) measurements in the range 200–600 nm were conducted in a Shimadzu UV-2401PC UV-Visible spectrometer using halogen and D2 lamp sources. FTIR spectra were measured to analyse the functional groups on the surface of samples with Bruker Alpha II FTIR spectrometer in the range of 500–4000 cm^{-1} . The emission and excitation PL spectra were measured on an Agilent Cary Eclipse fluorescence spectrometer with a xenon lamp as an excitation source. The PL lifetime was measured by an Edinburgh FLS1000 photoluminescence spectrometer.

Biological studies

Microbial cell viability and cell viability studies for $\text{NaRE}(\text{WO}_4)_2$ samples were conducted by serial dilution of test samples using *E. coli* (ATCC 25922), *S. aureus* (ATCC-25923) and human cervical cancer cell line HeLa cells, respectively. All compounds were dispersed in 50 mM phosphate buffer (pH = 7.0) and sonicated for 1 h prior to experiments.

Microbial cell viability assay

The microbial cytotoxicity of the given compounds was evaluated against a gram-negative bacteria, *Escherichia Coli* (ATCC 25922), and a gram-positive bacteria, *Staphylococcus aureus* (ATCC-25923) bacteria using the broth dilution method, as reported previously³⁶. Bacterial cells were pre-cultured in Luria-Bertani broth (LB broth) overnight at 37 °C. 1% of the bacterial suspension was reinoculated into a fresh LB broth to bring the bacterial cells to log phase and incubated at 37 °C. The bacterial cells were treated with the desired concentration of the inhibitors when the optical density (OD) of the bacterial culture reached 0.3–0.5. The viability of untreated cells was taken as a negative control. The optical density of the cells was estimated at different time intervals 6, 12, 24, 48, and 72 h using a Biotek 800 TS absorbance reader recorded at 600 nm.

Cell cytotoxicity studies by MTT assay

The cell cytotoxicity of all EG samples was examined using the HeLa cancer cell lines up to the highest concentration of 500 $\mu\text{g}/\text{ml}$ at five time points, 6, 12, 24, 48 and 72 h. Cells were cultured in Dulbecco's modified Eagle's medium (DMEM), supplemented with 10% (v/v) fetal bovine serum (FBS) and 1% (v/v) Penicillin-Streptomycin at 37 °C temperature in a humid atmosphere with 5% CO_2 . The cell viability was analyzed by MTT (3-[4,5-dimethylthiazol-2-yl]-2,5 diphenyl tetrazolium bromide) assay. Cells are grown to 80% confluency and further seeded with a cell density of 7000 cells per well onto a 96-well plate. After 24 h of culturing, cells were treated with compounds at the desired concentration. The untreated cells were taken as a negative control. The cells were further cultured for different time intervals 6, 12, 24, 48, and 72 h to analyze the effect of compounds on cell viability. After the desired time, 20 μL of 5 mg/ml MTT reagent was added to each well and incubated for 4 h. The medium was replaced, and 50 μL DMSO (dimethyl sulfoxide) was added to dissolve the formed formazan crystals. The absorbance was measured using an Envision plate reader at 595 nm, corresponding to the percentage of viable cells.

Result and discussion

Effect of synthesis methods

Crystal structure and morphology

There were considerable efforts to synthesize the samples by different methods to analyse the influence of the synthesis method on the particle size and morphologies of products¹⁵. Figure 1a–c illustrate the XRD patterns of synthesized samples, **S1**, **S2** and **S3** by solid-state reaction method, **H1**, **H2** and **H3** by hydrothermal method and **EG1**, **EG2** and **EG3** by a solvothermal method using EG as a solvent. X-ray diffraction patterns of all samples were indexed with a tetragonal phase and there were no additional peaks corresponding to secondary phase impurities. The samples display the scheelite structure with the space group $I4_1/a$ and are in agreement with reported studies on $\text{NaRE}(\text{WO}_4)_2$ compounds⁴. However, previously published results have shown 2–3 secondary impurity phases for all $\text{NaRE}(\text{WO}_4)_2$ samples obtained from the solid-state reaction method³⁵ whereas we could synthesize the phase pure samples from the same method without any secondary impurity phases (Fig. 1, Figs. S1, S4 and S7). In our solid-state reaction method, the finely ground powders are directly used for the annealing process instead of sintering the pellets. This modification might have yielded pure single-phase samples in our case. The scheelite crystal structure contains isolated WO_4 tetrahedra and edge-shared $(\text{Na}/\text{RE})\text{O}_8$ dodecahedra units such that W^{4+} cations occupy the 4a Wyckoff site whereas Na^+ and RE^{3+} cations are occupying the 4b Wyckoff site in a ratio of 1:1 and oxide anions are found at 16f site. The WO_4 tetrahedra and $(\text{Na}/\text{RE})\text{O}_8$ dodecahedra are characterized by a single W–O bond distance and two distinct Na/RE–O bond distances, respectively (Fig. 1d and Table S2 of supporting information). Further, WO_4 tetrahedra and $(\text{Na}/\text{RE})\text{O}_8$ dodecahedra in the structure are connected by bridging oxygen using Na/RE–O–W bridges. It is interesting to note that XRD peak intensities were sharply decreased in the solvothermal method when compared with the solid-state reaction and hydrothermal methods. Additionally, broad XRD peaks were obtained for all EG samples (**EG1**, **EG2** and **EG3**) synthesized by the solvothermal method. The XRD peak intensities and peak shape indicate high crystallinity of solid state and hydrothermal samples whereas the lower crystallinity and smaller crystallite size for solvothermal samples. The XRD pattern of all samples matches with the JCPDS card No 79-1118 for tetragonal $\text{NaLa}(\text{WO}_4)_2$ ($a=b=5.349$ Å, $c=11.628$ Å) as a reference. The Rietveld refinements were performed on samples using the GSAS-II program suite³⁷ and the obtained results were summarized in Figs. S1–S9 and Table S1 of supporting information. The crystallite sizes from the Rietveld refinement were found to be 123.6, 117.6 and 14.8 nm for **S1**, **H1** and **EG1**, 104.5, 105.3 and 28.0 nm for **S2**, **H2** and **EG2** and 64.5, 61.0 and 11.6 nm for **S3**, **H3** and **EG3**, respectively. The crystallite sizes determined from the Rietveld refinement were corrected for instrumental and strain effects. EG molecules behave as a capping agent in the solvothermal

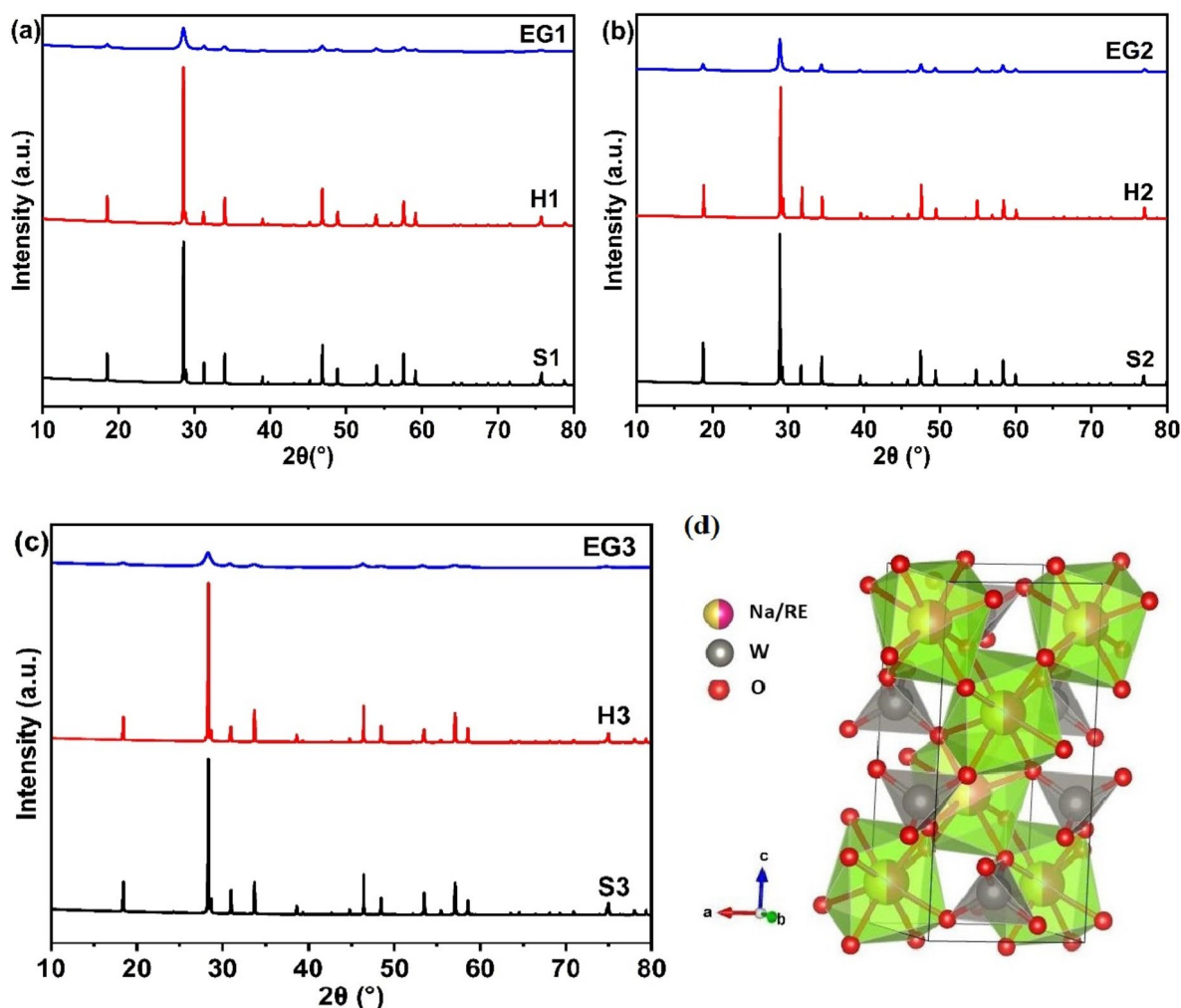


Fig. 1. XRD pattern of (a) $\text{NaSm}(\text{WO}_4)_2$ (S1, H1 and EG1) (b) $\text{NaHo}(\text{WO}_4)_2$ (S2, H2 and EG2) and (c) $\text{NaPr}(\text{WO}_4)_2$ (S3, H3 and EG3) samples. The notation S, H and EG denotes the sample preparation by solid-state reaction, hydrothermal and solvothermal methods, respectively. (d) Structural diagram of $\text{NaRE}(\text{WO}_4)_2$.

method and influence in controlling the surface morphology and particle size of synthesized samples, which provides the smaller-sized particles³⁸. Further, the viscosity and complexing behaviour of EG is also found to be crucial parameters to selecting EG as a solvent for controlling the particle size in solvothermal reactions. Indeed, similar results were demonstrated for $\text{NaEu}(\text{WO}_4)_2$ ¹⁵, and $\text{NaTb}(\text{WO}_4)_2$ ¹⁴, compounds during the solvothermal synthesis using EG.

Scanning electron microscopy (SEM) studies

The SEM micrographs of prepared samples by different methods are illustrated in Fig. 2. Indeed, the synthesis methods influence the surface morphology and particle size of prepared samples. SEM micrographs of S1, H1 and EG1 are displayed in Fig. 2a–c. S1 has agglomeration of spherical-shaped particles with an average size of 800 nm whereas H1 and EG1 have agglomeration of spherical particles of size 650 nm and 135 nm, respectively (Fig. 3a and Fig. S10). The particles have regular and uniform morphology throughout the sample. The samples, S2, H2 and EG2 (Fig. 2d–f) and S3, H3 and EG3 (Fig. 2g–i) have shown similar results. SEM study confirms that the solvothermal method provides smaller particles (Fig. 3) compared to the other two methods and results show the same trend as observed for the crystallite size determination from XRD. EDS spectrum and elemental mapping analysis were performed on all samples the presence of all constitutive elements and their uniform distribution (Fig. 4 and Figs. S11–S20). Additionally, there is a considerable influence of the rare-earth elements on the particle size distributions when compared between identical synthesis methods. In our studies, Ho^{3+} has resulted in a relatively smaller particle size distribution across all synthesis methods, which is followed by increased particle size distributions for Sm^{3+} and Pr^{3+} . Similar observations were also made during the hydrothermal synthesis of $\text{NaRE}(\text{WO}_4)_2$ in the literature and larger lattice distortions along the 'c' axis with decreasing RE ionic size could be the reason for it⁴.

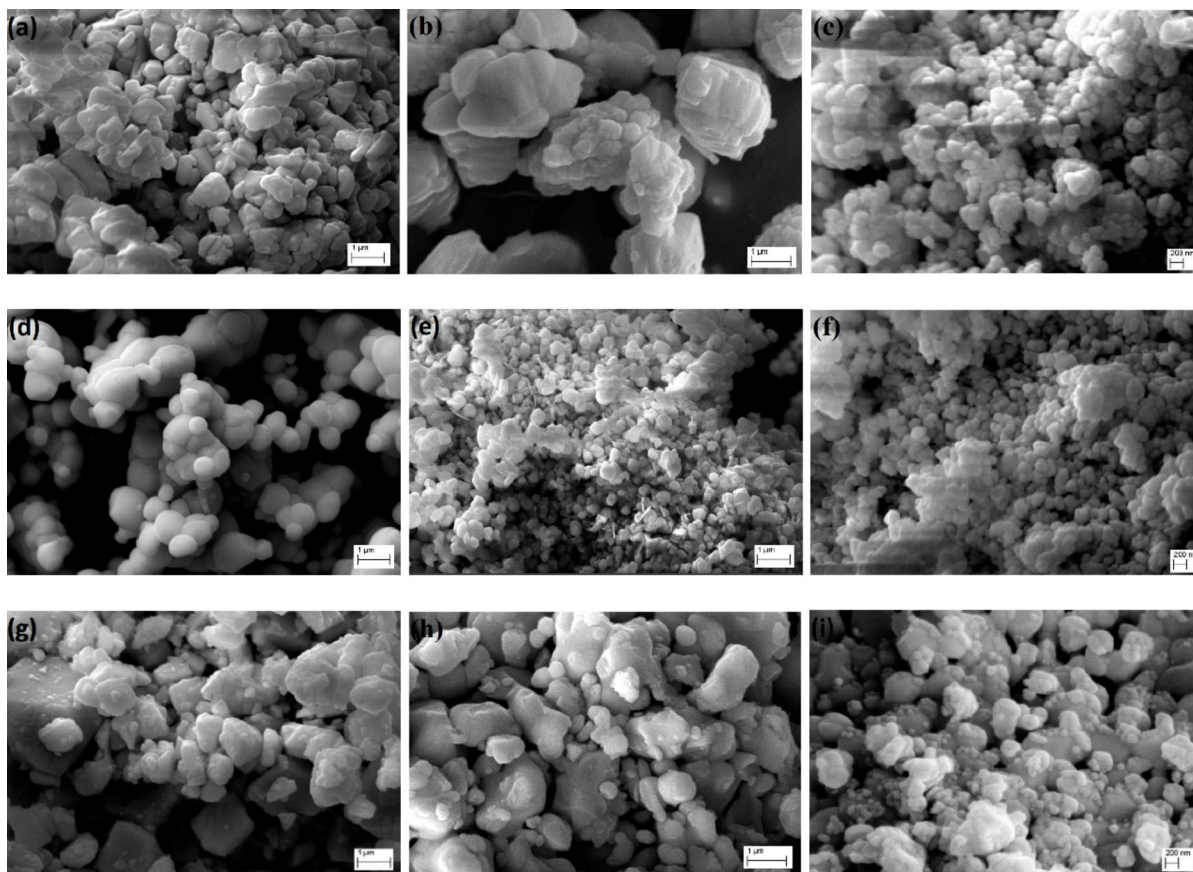


Fig. 2. SEM micrographs of (a) S1, (b) H1, (c) EG1, (d) S2, (e) H2, (f) EG2, (g) S3, (h) H3 and (i) EG3.

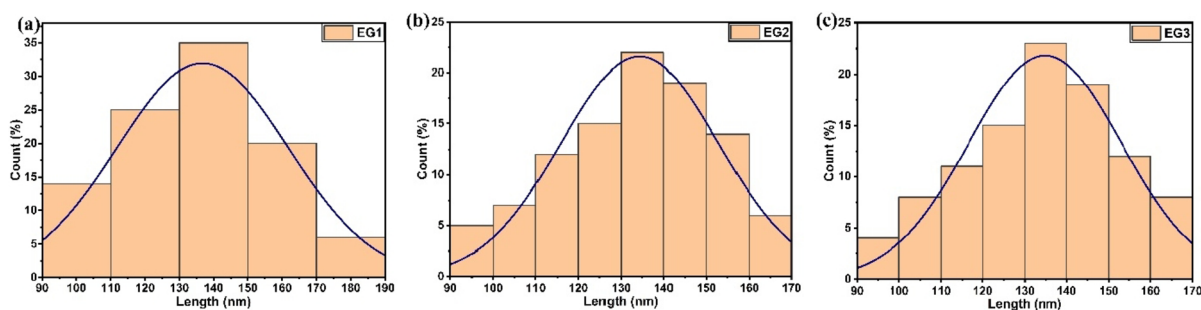


Fig. 3. Particle size distributions of as-synthesized (a) EG1, (b) EG2 and (c) EG3 samples.

Optical bandgap studies

A broad absorption peak around 250–300 nm in the UV-DRS spectra of $\text{NaRE}(\text{WO}_4)_2$ samples was assigned to the RE–O charge transfer band (CTB), the characteristic features of the Scheelite-like materials¹⁵. The other peaks were assigned to the intra-configurational f–f transitions. $\text{NaSm}(\text{WO}_4)_2$ samples from all synthesis methods exhibit absorption peaks at 377, 405, 420 and 466 nm corresponding to $^6\text{H}_{5/2} \rightarrow ^6\text{P}_{7/2}$, $^6\text{H}_{5/2} \rightarrow ^4\text{F}_{7/2}$, $^6\text{H}_{5/2} \rightarrow ^4\text{P}_{5/2}$ and $^6\text{H}_{5/2} \rightarrow ^4\text{I}_{13/2}$ transitions respectively^{24,25}. Similarly, $\text{NaHo}(\text{WO}_4)_2$ samples show absorption peaks 360, 398, 418 and 455 nm corresponding to $^5\text{I}_8 \rightarrow ^3\text{H}_5$, $^5\text{I}_8 \rightarrow ^5\text{G}_4$, $^5\text{I}_8 \rightarrow ^5\text{G}_5$ and $^5\text{I}_8 \rightarrow ^5\text{G}_6$ transitions, respectively^{40,41}. $\text{NaPr}(\text{WO}_4)_2$ samples demonstrate absorption peaks at 449, 473 and 487 nm corresponding to the $^3\text{H}_4 \rightarrow ^3\text{P}_2$, $^3\text{H}_4 \rightarrow ^3\text{P}_1$ and $^3\text{H}_4 \rightarrow ^3\text{P}_0$ transitions, respectively^{42,43}. The positions of intra-configurational f–f transitions for RE^{3+} ions remain the same indicating identical crystal structure and crystallographic site occupancy for RE^{3+} ions across different synthesis methods.

The determination of the optical bandgap was performed based on the Kubelka-Munk function (Tauc plot) using the UV-DRS spectra for all samples. The energy band gaps for $\text{NaRE}(\text{WO}_4)_2$ (RE = Sm^{3+} , Ho^{3+} and Pr^{3+}) were in the range varying from 4.25 to 4.75 eV as depicted in Fig. 5 and listed in Table S3 of supporting information. The band gap values for EG samples were high compared to those of respective solid state and hydrothermal

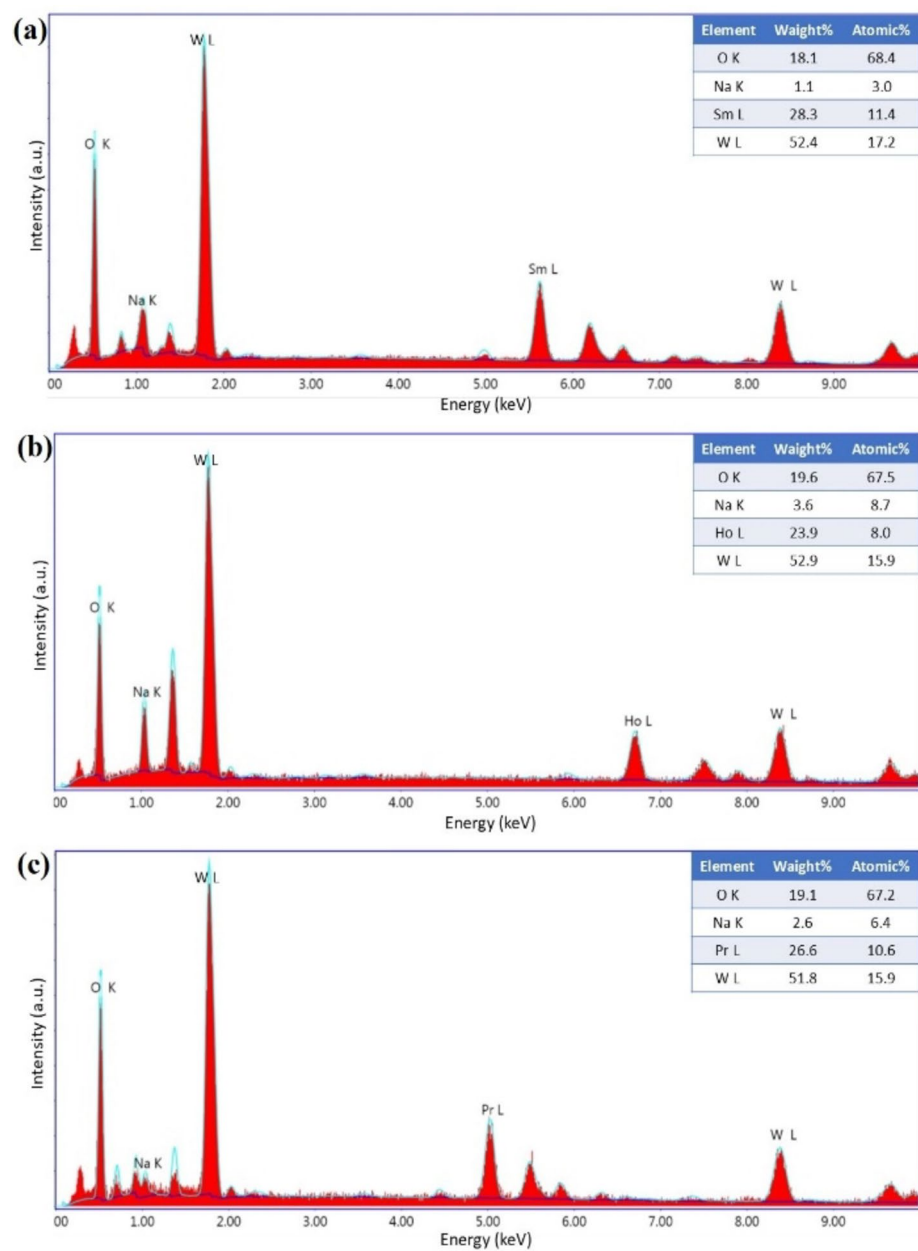


Fig. 4. EDS spectrum of (a) EG1, (b) EG2 and (c) EG3 samples.

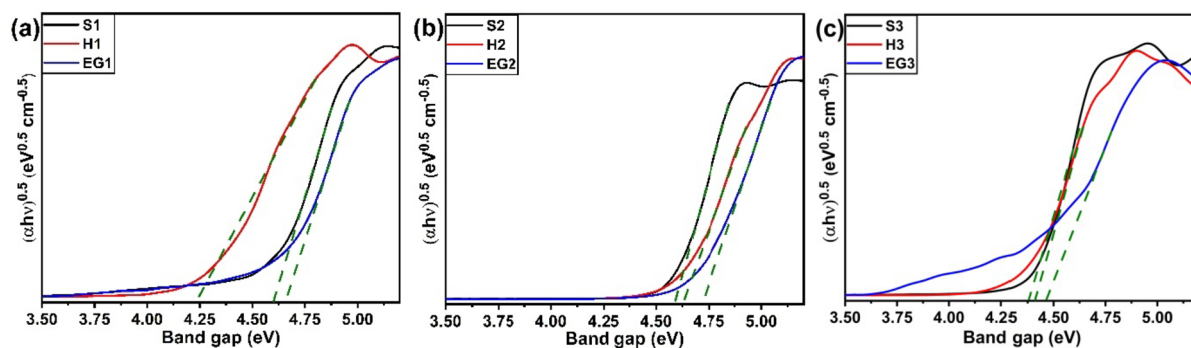


Fig. 5. Tauc plot of (a) $\text{NaSm}(\text{WO}_4)_2$ [S1/H1/EG1], (b) $\text{NaHo}(\text{WO}_4)_2$ [S2/H2/EG2] and (c) $\text{NaPr}(\text{WO}_4)_2$ [S3/H3/EG3] determined from the Tauc plot.

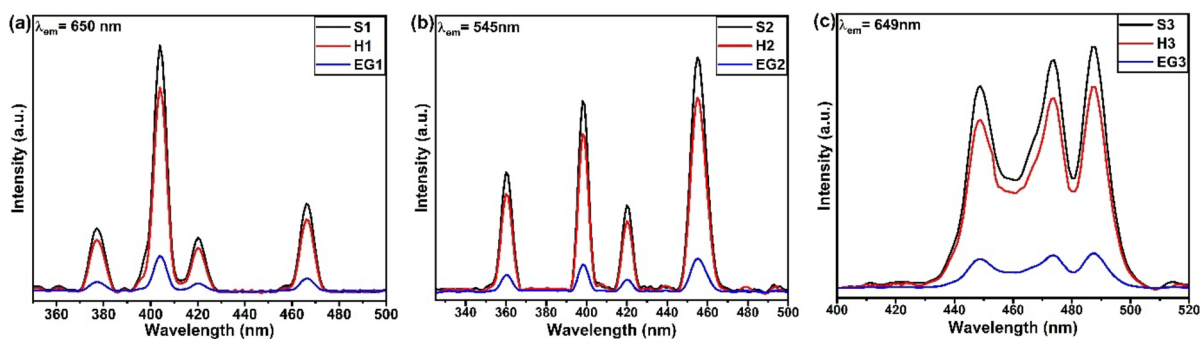


Fig. 6. Excitation spectra of (a) $\text{NaSm}(\text{WO}_4)_2$ [S1/H1/EG1] (b) $\text{NaHo}(\text{WO}_4)_2$ [S2/H2/EG2] and (c) $\text{NaPr}(\text{WO}_4)_2$ [S3/H3/EG3].

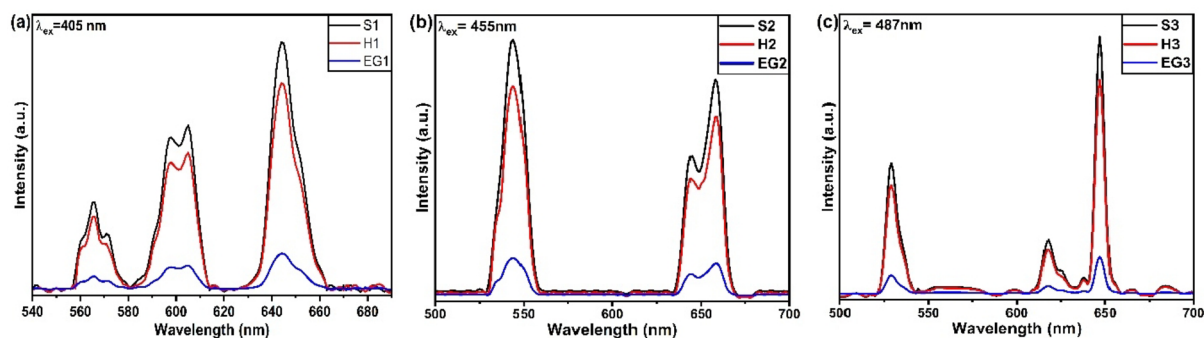


Fig. 7. Emission spectra of (a) $\text{NaSm}(\text{WO}_4)_2$ [S1/H1/EG1], (b) $\text{NaHo}(\text{WO}_4)_2$ [S2/H2/EG2] and (c) $\text{NaPr}(\text{WO}_4)_2$ [S3/H3/EG3].

samples. The increase in the optical bandgap for EG samples is due to smaller particle size in the solvothermal method which is further consistent with XRD and SEM results. EG solvent used in the solvothermal method behaves as a capping and complexing agent in the synthesis and restricts the growth of particles. It is known that the size reduction in particles would affect the energy levels³⁹. Hence, the synthesis method could control the particle size and subsequent optical bandgap of materials. The bandgap tuning of the material by controlling the synthesis methods is useful for obtaining exotic physical properties due to quantum and surface effects³⁹. It could have potential applications in catalysis, optoelectronics, cell imaging, and theranostic applications.

Photoluminescence studies

Figure 6 shows the comparison of luminescence excitation of $\text{NaRE}(\text{WO}_4)_2$ ($\text{RE} = \text{Sm}^{3+}$, Ho^{3+} and Pr^{3+}) prepared by three different synthesis methods. The maximum PL emission was noticed for the samples obtained by the solid reaction method whereas the lowest PL intensity was seen for the solvothermal samples. The lower PL intensity for the solvothermal samples could be explained by the existence of surface defects and organic functional groups such as $-\text{CH}$ and $-\text{OH}$ groups from EG in as-prepared samples and it was supported by the FTIR spectra in the range $500\text{--}4000\text{ cm}^{-1}$ (Fig. S21)¹⁵. The vibrational frequencies corresponding to $-\text{CH}$ and $-\text{OH}$ groups were observed in as-synthesized EG samples and they were found to be absent after the calcination at $600\text{ }^\circ\text{C}$ for 12 h. As expected, the position of vibrational frequencies corresponding to the W–O–W stretching remains unaltered during the calcination process.

Excitation spectra were further monitored at different emissions for all samples clearly indicating that RE tungstate materials can be excited using several wavelengths. Figure 6a shows the excitation spectra of $\text{NaSm}(\text{WO}_4)_2$ samples for the PL emission at 650 nm ^{24,25}. This gives an intense peak at 405 nm corresponds to ${}^6\text{H}_{5/2} \rightarrow {}^4\text{F}_{7/2}$ transition and smaller peaks at 377 , 420 and 466 nm corresponding to ${}^6\text{H}_{5/2} \rightarrow {}^6\text{P}_{7/2}$, ${}^6\text{H}_{5/2} \rightarrow {}^4\text{P}_{5/2}$ and ${}^6\text{H}_{5/2} \rightarrow {}^4\text{I}_{13/2}$ transitions respectively^{24,25}. Figure 6b displays the excitation spectra of $\text{NaHo}(\text{WO}_4)_2$ samples for the PL emission at 545 nm ^{40,41}. It results in excitation peaks at 360 , 398 , 418 and 455 nm corresponding to ${}^5\text{I}_8 \rightarrow {}^3\text{H}_5$, ${}^5\text{I}_8 \rightarrow {}^3\text{G}_4$, ${}^5\text{I}_8 \rightarrow {}^5\text{G}_5$ and ${}^5\text{I}_8 \rightarrow {}^5\text{G}_6$, respectively^{40,41}. The excitation spectra of $\text{NaPr}(\text{WO}_4)_2$ samples for the PL emission at 649 nm in Fig. 5c. The peaks at 449 , 473 nm and intense peak at 487 nm are corresponding to ${}^3\text{H}_4 \rightarrow {}^3\text{P}_2$, ${}^3\text{H}_4 \rightarrow {}^3\text{P}_1$ and ${}^3\text{H}_4 \rightarrow {}^3\text{P}_0$ transitions, respectively^{42,43}. It is interesting to note that solid-state reaction method samples (S1, S2 and S3) show more intense PL peaks than the samples from the other two synthesis methods. This could be attributed to higher crystallinity and fewer surface defects of samples in the solid-state synthesis which minimizes non-radiative transitions.

Figure 7 shows the PL emission spectra of $\text{NaRE}(\text{WO}_4)_2$ ($\text{RE} = \text{Sm}^{3+}$, Ho^{3+} and Pr^{3+}) samples. This also follows a similar trend as discussed above. The PL emission intensity decreases with decreasing the particle

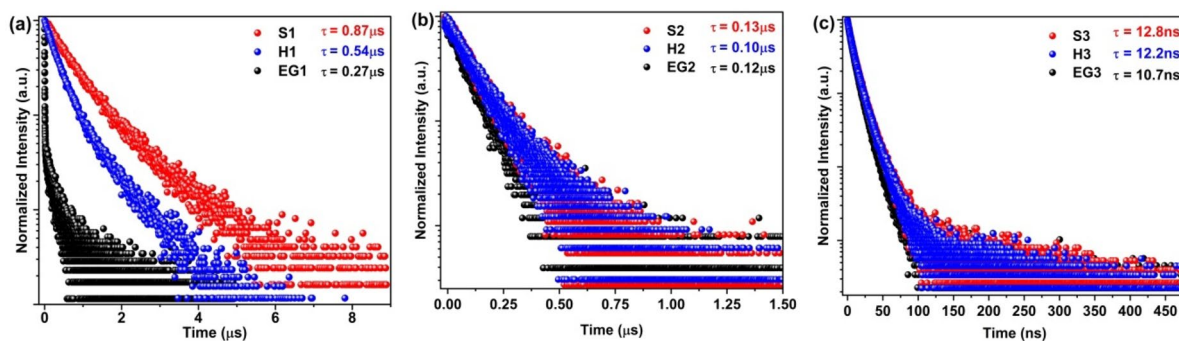


Fig. 8. PL decay curves of (a) $\text{NaSm}(\text{WO}_4)_2$ [S1/H1/EG1], (b) $\text{NaHo}(\text{WO}_4)_2$ [S2/H2/EG2] and (c) $\text{NaPr}(\text{WO}_4)_2$ [S3/H3/EG3].

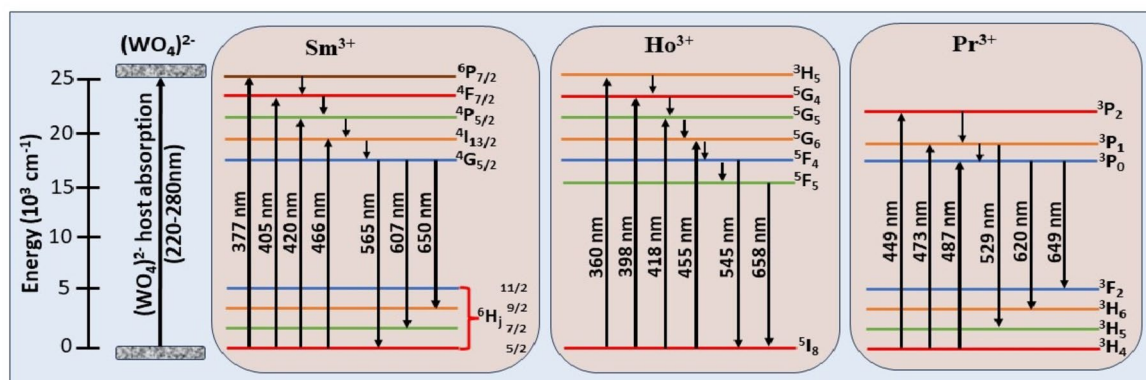


Fig. 9. Energy level diagram of Sm^{3+} , Ho^{3+} and Pr^{3+} in $\text{NaRE}(\text{WO}_4)_2$.

size of samples. Figure 7a displays the PL emission spectra of $\text{NaSm}(\text{WO}_4)_2$ under the 405 nm excitation. The emission peak centred at 650 nm corresponds to the ${}^4\text{G}_{5/2} \rightarrow {}^6\text{H}_{9/2}$ transition of Sm^{3+} . Two other peaks at 565 and 607 nm correspond to the ${}^4\text{G}_{5/2} \rightarrow {}^6\text{H}_{5/2}$ and ${}^4\text{G}_{5/2} \rightarrow {}^6\text{H}_{7/2}$ transitions, respectively^{24,25}. Figure 7b illustrates the PL emission spectra of $\text{NaHo}(\text{WO}_4)_2$ under 455 nm excitation. Two emission peaks at 545 nm correspond to the ${}^5\text{F}_4 \rightarrow {}^5\text{I}_8$ transition and 658 nm correspond to the ${}^5\text{F}_5 \rightarrow {}^5\text{I}_8$ transition^{40,41} of Ho^{3+} . Similarly, the PL emission spectra of $\text{NaPr}(\text{WO}_4)_2$ under 487 nm excitation are shown in Fig. 7c. The emission peaks centred at 529, 620 nm and intense peak at 649 nm are corresponding to the ${}^3\text{P}_1 \rightarrow {}^3\text{H}_5$, ${}^3\text{P}_0 \rightarrow {}^3\text{H}_6$ and ${}^3\text{P}_0 \rightarrow {}^3\text{F}_2$ transitions of Pr^{3+} , respectively^{42,43}. The PL emission lifetime (Fig. 8) on $\text{NaRE}(\text{WO}_4)_2$ (RE = Sm^{3+} , Ho^{3+} and Pr^{3+}) were performed to determine the performance of synthesized samples and to understand non-radiative quenching pathways in the structure. All samples have shown a lifetime in the range from μs to ns. From the room temperature PL decay profile (Fig. 8) shows an average lifetime of 0.27–0.87 μs , 0.10–0.13 μs , and 10.7–12.8 ns for $\text{NaSm}(\text{WO}_4)_2$, $\text{NaHo}(\text{WO}_4)_2$ and $\text{NaPr}(\text{WO}_4)_2$, respectively. On the basis of above mentioned PL spectral measurements, the energy level diagram of Sm^{3+} , Ho^{3+} and Pr^{3+} in $\text{NaRE}(\text{WO}_4)_2$ with possible excitation and emission pathways is shown in Fig. 9.

Temperature dependent PL properties

As described in the previous section, the lower PL intensity was observed for the solvothermal samples where the smaller-size particles were obtained. However, the smaller particles with higher PL emission are required for most of practical applications such as bio-imaging. Thus, the PL intensity of EG1, EG2 and EG3 samples need to be enhanced without altering their particle size. Systematic studies have demonstrated that the calcination process enhances the PL emission of the sample^{15,44}. Thus, as-synthesized EG samples were systematically calcined at various temperatures such as 300, 400, 500 and 600 °C for 12 h to evaluate the effect of calcination temperature on the particle size and PL properties.

Figure 10 displays the XRD pattern of EG1, EG2 and EG3 calcined at 300, 400, 500 and 600 °C for 12 h. Indeed, the original crystal structure and phase were preserved during the calcination as shown by XRD peaks. This indicates the high-temperature stability of $\text{NaRE}(\text{WO}_4)_2$ prepared by the solvothermal method. However, the XRD peak intensity enhances with the calcination temperature which strongly suggests improvement in the crystallinity of EG samples. The SEM micrographs of calcined EG samples at 600 °C for 12 h are shown in Fig. 11. There were no significant changes in the particle size distribution with the calcination temperature. The

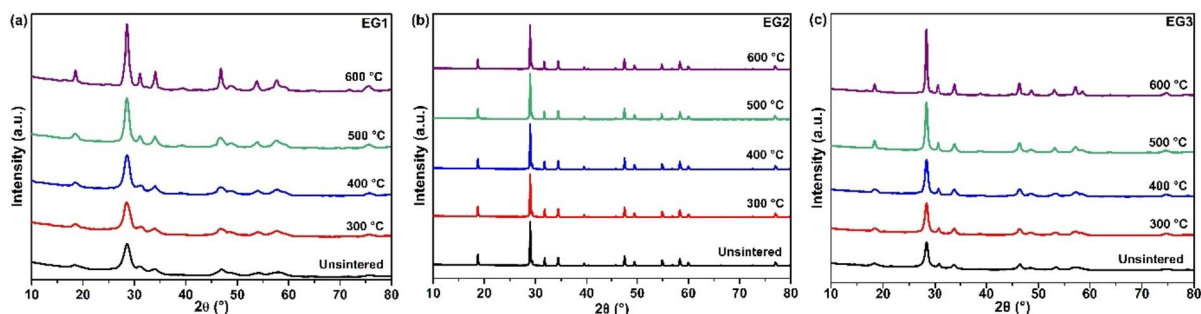


Fig. 10. XRD pattern of (a) EG1, (b) EG2 and (c) EG3 at various calcination temperatures from 300 to 600 °C.

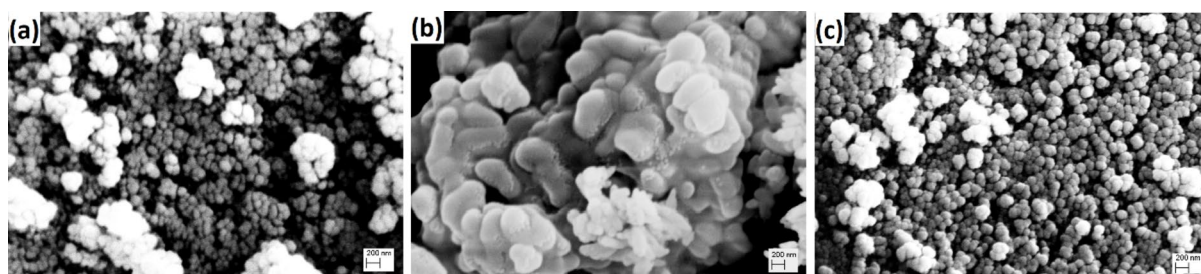


Fig. 11. SEM micrographs of (a) EG1, (b) EG2 and (c) EG3 after calcination at 600 °C for 12 h.

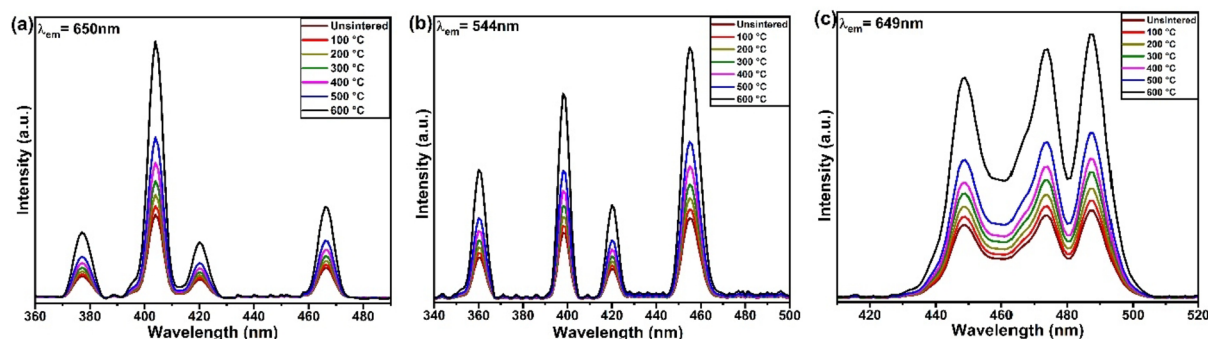


Fig. 12. Excitation spectra of (a) EG1, (b) EG2 and (c) EG3 at different calcination temperature.

homogeneous particle distributions with small surface agglomeration were observed. The average particle size after calcination was about ~100–140 nm which was comparable to as-synthesized samples without calcination.

The excitation and emission PL spectra of calcined EG1, EG2 and EG3 samples at various calcination temperatures are shown in Figs. 12 and 13. A systematic enhancement in the PL emission intensity was demonstrated by increasing the calcination temperature for EG samples. The PL intensity of the calcined sample at 600 °C was tripled to that of the samples without calcinating. As-synthesized samples have low PL intensity due to the presence of –CH and –OH organic moieties on the surface of particles which result in increased non-radiative transitions. The calcination will improve the crystallinity of samples and reduce microstrain in the sample. Further, disappearance of –CH and –OH organic moieties from the calcination process might also contribute to increasing PL intensities of calcined samples. Indeed, the PL emission intensity could be improved for EG samples by retaining their particle size and crystal structure through a suitable calcination process.

CIE chromaticity studies

The estimated CIE-X and CIE-Y coordinate values for NaSm(WO₄)₂ [S1/H1/EG1], NaHo(WO₄)₂ [S2/H2/EG2] and NaPr(WO₄)₂ [S3/H3/EG3] were found to be 0.60, 0.39; 0.36, 0.63 and 0.46, 0.53 respectively and shown in Fig. 14. Thermally treated EG1, EG2 and EG3 samples also displayed identical CIE coordinates at all temperatures. Indeed, the CIE chromaticity coordinates were independent of the synthesis method and calcination temperature. The CIE coordinates obtained for NaSm(WO₄)₂ were located in the red-orange region and close to reported values for NaGa_{1-x}Eu_x(WO₄)₂ in the literature²². Similarly, the CIE values for NaHo(WO₄)₂

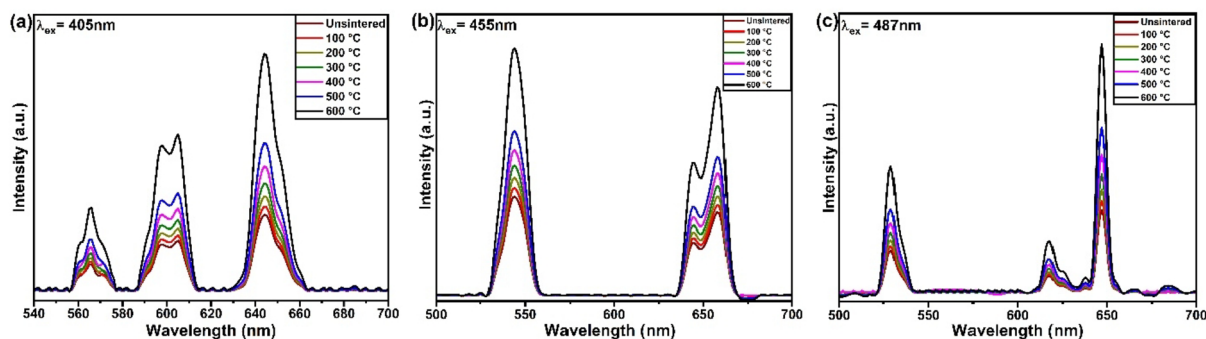


Fig. 13. Emission spectra of (a) EG1, (b) EG2 and (c) EG3 at different calcination temperatures.

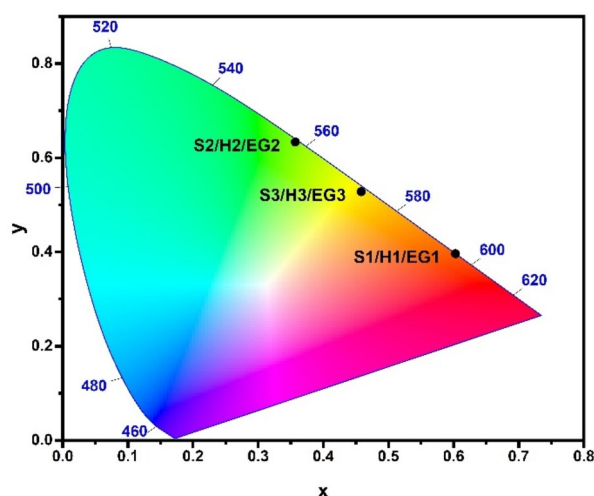


Fig. 14. CIE chromaticity diagram of (a) $\text{NaSm}(\text{WO}_4)_2$ [S1/H1/EG1], (b) $\text{NaHo}(\text{WO}_4)_2$ [S2/H2/EG2] and (c) $\text{NaPr}(\text{WO}_4)_2$ [S3/H3/EG3].

were closer to the commercially available $\text{Y}_2\text{O}_3:\text{Tb}^{3+}$ green phosphor¹⁷ and other reported green phosphors^{15,45}. The CIE coordinates for $\text{NaPr}(\text{WO}_4)_2$ were determined in the orange region which is close to the Al-doped ZnO phosphor⁴⁶.

Biological studies

Cell viability studies

The microbial cell viability experiments were carried out on a gram-negative (*E. coli*) and a gram-positive (*S. aureus*) bacterium to examine the biocompatibility of synthesized samples as depicted in Figs. 15 and 16. Indeed, EG1, EG2 and EG3 were utilized for the biological studies due to their smaller particle size. The microbial growth without nanoparticles was taken as the control growth and considered as 100% viable. The dose-dependent study at five-time points till 72 h was carried out on EG1, EG2 and EG3 samples and results suggest the non-toxicity of $\text{NaRe}(\text{WO}_4)_2$ ($\text{RE} = \text{Sm}^{3+}$, Ho^{3+} and Pr^{3+}) towards microbial growth in comparison with the controlled bacterial growth. The microbial cells were more than 90% viable at the highest concentration of 500 $\mu\text{g}/\text{ml}$ at 48 and 72 h for all EG samples as demonstrated in Figs. 15 and 16. Hence, these compounds may not exhibit major adversary effects on the cell membrane or the subcellular components. Indeed, cell viability results are comparable to similar studies on $\text{NaEu}(\text{WO}_4)_2$ ¹⁵, $\text{NaTb}(\text{WO}_4)_2$ ¹⁴, and $\text{NaGd}(\text{MoO}_4)_2$ ⁴⁷, compounds.

Cell cytotoxicity studies

The cell cytotoxicity experiments were conducted on the human cervix carcinoma HeLa cell line. The cells were treated dose-dependently at five time points, 6, 12, 24, 48 and 72 h. The HeLa cells without nanoparticles are taken as the control cells and considered 100% viable. The present study highlighted that all three EG compounds do not show a cytotoxic effect on the cell, as shown by the higher cell density percentage. The cells under the study were more than 90% viable at the highest concentration of 500 $\mu\text{g}/\text{ml}$ at 48 and 72 h for all three EG samples as displayed in Fig. 17. Additionally, stimulated cell viability was observed at certain time points, especially at higher concentrations, suggesting that $\text{NaRe}(\text{WO}_4)_2$ ($\text{RE} = \text{Sm}^{3+}$, Ho^{3+} and Pr^{3+}) samples were compatible with cell growth and proliferation.

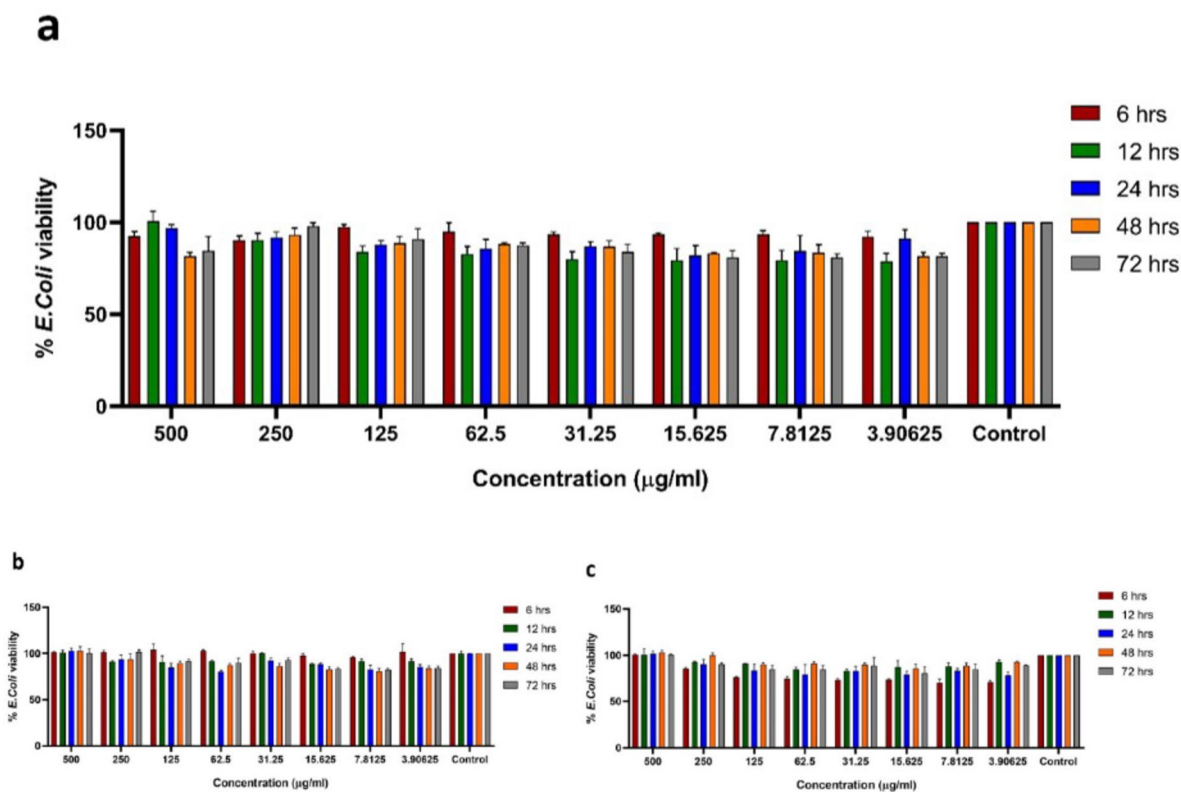


Fig. 15. Microbial cell viability studies on *E. coli* using (a) EG1, (b) EG2 and (c) EG3 with time. The control (negative) is the untreated cells viability without nanoparticles and is considered as 100%. The results are the mean of triplicated values.

Conclusions

The phase pure double tungstates, $\text{NaRE}(\text{WO}_4)_2$ ($\text{RE} = \text{Sm}^{3+}$, Ho^{3+} and Pr^{3+}) were synthesized by solid-state reaction, hydrothermal and solvothermal methods to analyse the influence of the synthesis methods on the particle size and subsequent biocompatibility and PL properties. The XRD and SEM confirm the formation of the smallest size particles from the solvothermal method where ethylene glycol molecules act as a capping agent and restrict the growth of particles. The crystallite and particle sizes of samples obtained from the solvothermal method are about 11–26 nm and 135–140 nm, respectively. The PL emission intensity was minimal for as-synthesized solvothermal samples compared to other two methods. All samples have shown an average lifetime in the range from 0.87 μs to 10.7 ns. The PL intensity was increased with increasing the calcination temperature for the solvothermal samples. The smaller particle size samples are more useful for biological applications. Thus, the microbial cell viability and cytotoxicity towards cancer cells were performed on the solvothermal samples using *E. coli*, *S. aureus* and HeLa cells, respectively and $\text{NaRE}(\text{WO}_4)_2$ ($\text{RE} = \text{Sm}^{3+}$, Ho^{3+} and Pr^{3+}) demonstrated good biocompatibility and comparable with similar family of tungstate compounds. These biocompatible double tungstates could be doped with suitable RE ions to enhance their PL properties for bio-imaging applications.

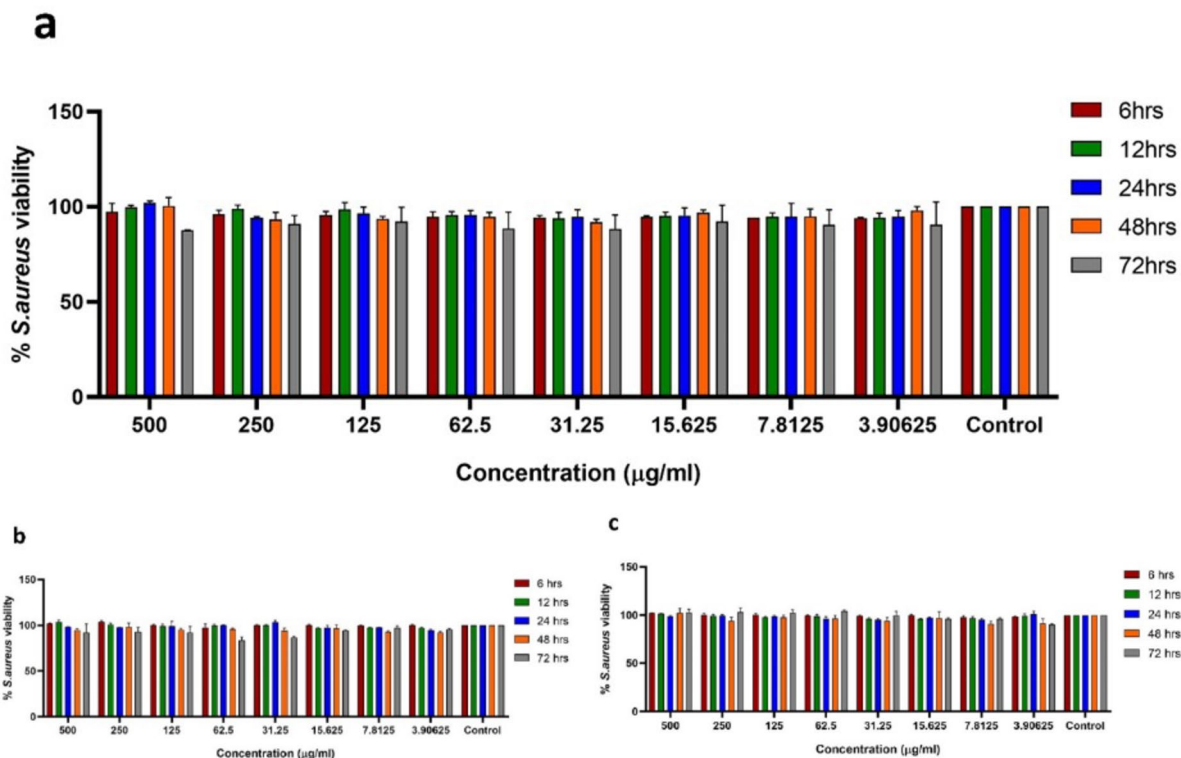


Fig. 16. Microbial cell cytotoxicity studies on *S. aureus*. (a) EG1, (b) EG2 and (c) EG3 with time. The control (negative) is the untreated cells' viability without nanoparticles and is considered as 100%. The results are the mean of triplicated values.

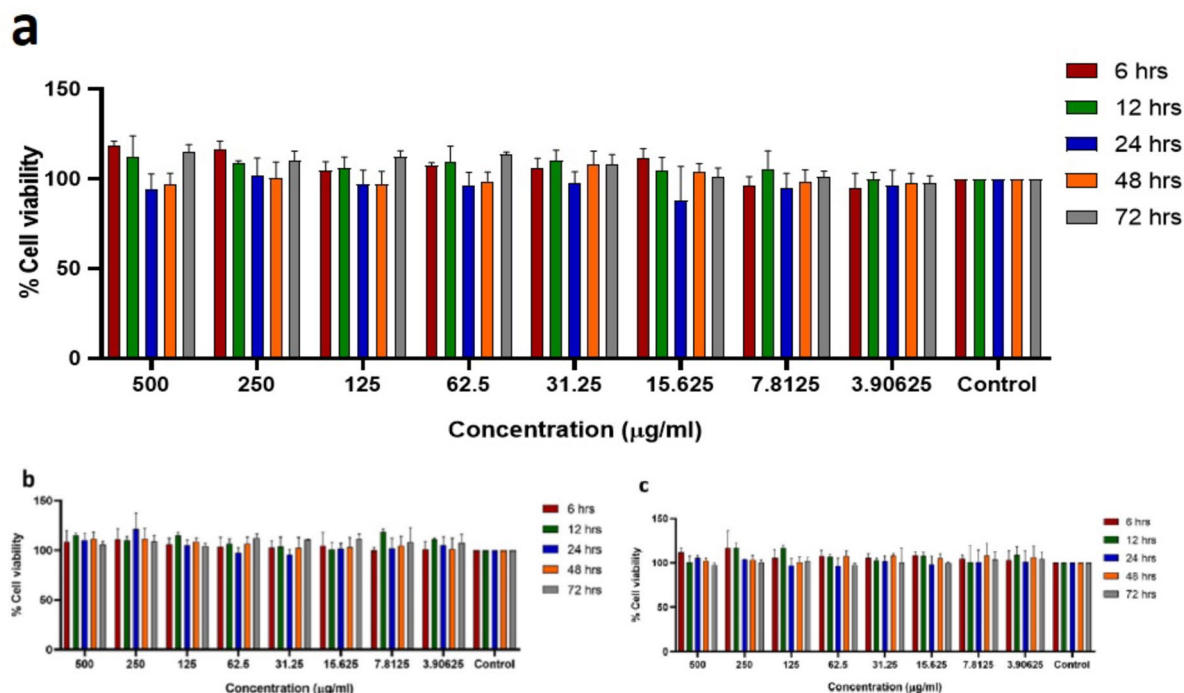


Fig. 17. Cell cytotoxicity studies. (a) EG1, (b) EG2 and (c) EG3 with time. The control (negative) is the viability of the cells without any nanoparticles considered as 100%. The results are the mean of triplicated values.

Data availability

All data used in this article are available for readers from the corresponding author upon a request.

Received: 18 September 2024; Accepted: 5 March 2025

Published online: 01 July 2025

References

- Kaczmarek, A. M. & Van Deun, R. Rare Earth tungstate and molybdate compounds—from 0D to 3D architectures. *Chem. Soc. Rev.* **42**, 8835–8848 (2013).
- Gupta, I., Singh, S., Bhagwan, S. & Singh, D. Rare Earth (RE) doped phosphors and their emerging applications: A review. *Ceram. Int.* **47**, 19282–19303 (2021).
- Liu, X., Hou, W., Yang, X. & Liang, J. Morphology controllable synthesis of $\text{NaLa}(\text{WO}_4)_2$: the morphology dependent photoluminescent properties and single-phased white light emission of $\text{NaLa}(\text{WO}_4)_2$: $\text{Eu}^{3+}/\text{Tb}^{3+}/\text{Tm}^{3+}$. *CrystEngComm* **16**, 1268–1276 (2014).
- Shi, X. et al. Facile hydrothermal crystallization of $\text{NaLn}(\text{WO}_4)_2$ (Ln=La-Lu, and Y), phase/morphology evolution, and photoluminescence. *Sci. Technol. Adv. Mater.* **18**, 741–754 (2017).
- Wang, H. et al. Optical properties of Dy^{3+} ions in sodium gadolinium tungstates crystal. *J. Lumin.* **126**, 452–458 (2007).
- Shao, Q., Li, H., Wu, K., Dong, Y. & Jiang, J. Photoluminescence studies of red-emitting $\text{NaEu}(\text{WO}_4)_2$ as a near-UV or blue convertible phosphor. *J. Lumin.* **129**, 879–883 (2009).
- Yun, X., Zhou, J., Zhu, Y., Li, X. & Xu, D. Up-conversion luminescence and optical temperature sensing properties of Ho^{3+} -doped double-tungstate $\text{LiYb}(\text{WO}_4)_2$ phosphors. *J. Mater. Sci. Mater. Electron.* **32**, 17990–18001 (2021).
- Cano-Torres, J. M. et al. Epitaxial growth of $\text{NaGd}_{0.935}\text{Yb}_{0.065}(\text{WO}_4)_2$ layers on lattice matched tetragonal double tungstate substrates for ultrafast thin disk lasers. *Cryst. Growth Des.* **11**, 1807–1813 (2011).
- Durairajan, A., Thangaraju, D., Balaji, D., Moorthy & Babu Sol-gel synthesis and characterizations of crystalline $\text{NaGd}(\text{WO}_4)_2$ powder for anisotropic transparent ceramic laser application. *Opt. Mater.* **35**, 740–743 (2013).
- Vázquez-Córdova, S. A. et al. High optical gain in erbium-doped potassium double tungstate channel waveguide amplifiers. *Opt. Express* **26**, 6260–6266 (2018).
- Laguna, M. et al. Synthesis, functionalization and properties of uniform europium-doped sodium lanthanum tungstate and molybdate ($\text{NaLa}(\text{XO}_4)_2$, X=Mo,W) probes for luminescent and X-ray computed tomography bioimaging. *J. Colloid Interface Sci.* **554**, 520–530 (2019).
- Perera, S. S. & Rabuffetti, F. A. Dysprosium-activated scheelite-type oxides as thermosensitive phosphors. *J. Mater. Chem. C* **7**, 7601–7608 (2019).
- Wang, Z. et al. White light tuning and temperature sensing of $\text{NaLu}(\text{WO}_4)_2$: Ln^{3+} up-converting phosphor. *RSC Adv.* **12**, 10489–10495 (2022).
- Munirathnappa, A. K. et al. Scheelite like $\text{NaTb}(\text{WO}_4)_2$ nanoparticles: green fluorescence and in vitro cell imaging applications. *Mater. Sci. Eng. C* **106**, 110182 (2020).
- Munirathnappa, A. K., Sinha, K. A., Sundaram, N. G. & A. K. & Effect of solvent on the red luminescence of novel lanthanide $\text{NaEu}(\text{WO}_4)_2$ nanophosphor for theranostic applications. *Cryst. Growth Des.* **18**, 253–263 (2018).
- Gai, S., Li, C., Yang, P. & Lin, J. Recent progress in rare Earth micro/nanocrystals: soft chemical synthesis, luminescent properties, and biomedical applications. *Chem. Rev.* **114**, 2343–2389 (2014).
- Yang, M. et al. Multifunctional luminescent nanomaterials from $\text{NaLa}(\text{MoO}_4)_2$: $\text{Eu}^{3+}/\text{Tb}^{3+}$ with tunable decay lifetimes, emission colors and enhanced cell viability. *Sci. Rep.* **5**, 11844 (2015).
- Peter, A. J. & Banu, I. B. S. Synthesis and luminescence properties of $\text{NaLa}(\text{WO}_4)_2$: Eu^{3+} phosphors for white LED applications. *J. Mater. Sci. Mater. Electron.* **28**, 8023–8028 (2017).
- Tang, Y. et al. Hydrothermal synthesis of $\text{NaLa}(\text{WO}_4)_2$: Eu^{3+} octahedrons and tunable luminescence by changing Eu^{3+} concentration and excitation wavelength. *J. Mater. Sci. Mater. Electron.* **28**, 1301–1306 (2017).
- Gu, J., Zhu, Y., Li, H., Zhang, X. & Qian, Y. Uniform Ln^{3+} (Eu^{3+} , Tb^{3+}) doped $\text{NaLa}(\text{WO}_4)_2$ nanocrystals: synthesis, characterization, and optical properties. *J. Solid State Chem.* **183**, 497–503 (2010).
- Wang, H. et al. A novel red phosphor $\text{Li}_x\text{Na}_{1-x}\text{Eu}(\text{WO}_4)_2$ solid solution: influences of Li/Na ratio on the microstructures and luminescence properties. *J. Lumin.* **201**, 364–371 (2018).
- Durairajan, A. et al. Photoluminescence properties of sub-micron $\text{NaGd}_{1-x}\text{Eu}_x(\text{WO}_4)_2$ red phosphor for solid state lightings application: derived by different synthesis routes. *Superlatt Microstruct.* **93**, 308–321 (2016).
- Rasu, K. K., Balaji, D. & Babu, S. M. Spectroscopic properties of Eu^{3+} : $\text{KLa}(\text{WO}_4)_2$ novel red phosphors. *J. Lumin.* **170**, 547–555 (2016).
- Li, M. et al. Tunable emission of single-phased $\text{NaY}(\text{WO}_4)_2$: Sm^{3+} phosphor based on energy transfer. *Ceram. Int.* **43**, 6751–6757 (2017).
- Durairajan, A. et al. Sol-gel synthesis and photoluminescence analysis of Sm^{3+} : $\text{NaGd}(\text{WO}_4)_2$ phosphors. *J. Lumin.* **170**, 743–748 (2016).
- Wang, H. et al. Optical properties of Ho^{3+} -doped $\text{NaGd}(\text{WO}_4)_2$ crystal for laser materials. *J. Alloys Compd.* **431**, 277–281 (2007).
- Xiong, F. B. et al. Luminescent properties of deep red light-emitting phosphors $\text{NaGd}(\text{WO}_4)_2$: Pr^{3+} for blue LED. *Opt. Mater.* **42**, 394–398 (2015).
- Zhang, W. et al. Synthesis and photoluminescent features of Eu^{3+} -doped $\text{NaGd}(\text{WO}_4)_2$ nanophosphors. *Mater. Res. Bull.* **122**, 110689 (2020).
- Liao, J., Qiu, B. & Lai, H. Synthesis and luminescence properties of Tb^{3+} : $\text{NaGd}(\text{WO}_4)_2$ novel green phosphors. *J. Lumin.* **129**, 668–671 (2009).
- Liu, X., Xiang, W., Chen, F., Hu, Z. & Zhang, W. Synthesis and photoluminescence characteristics of Dy^{3+} doped $\text{NaY}(\text{WO}_4)_2$ phosphors. *Mater. Res. Bull.* **48**, 281–285 (2013).
- Xiong, F. B., Lin, H. F., Wang, L. J., Meng, X. G. & Zhu, W. Z. White light emission in host-sensitized Dy^{3+} -single-doped $\text{NaIn}(\text{WO}_4)_2$ phosphors. *Phys. B Condens. Matter* **459**, 41–45 (2015).
- Tan, S., Wang, X., Zhao, Y., Li, Y. & Yao, X. Strong luminescence intensity and high temperature sensitivity of Er^{3+} -doped $\text{KYb}(\text{MoO}_4)_2$ phosphors optimized by codoping trivalent ions. *J. Lumin.* **257**, 119747 (2023).
- Devi, S., Singhaal, R., Sen, C. & Sheikh, H. N. Luminescent and photocatalytic activity of $\text{NaGd}(\text{MoO}_4)_2$: $\text{Dy}^{3+}/\text{Eu}^{3+}$ and $\text{NaGd}(\text{WO}_4)_2$: $\text{Dy}^{3+}/\text{Eu}^{3+}$ nanorods for efficient sensing and degradation of the antibiotic drug, Nitrofurantoin. *New J. Chem.* **47**, 4949–4963 (2023).
- Li, A. et al. Solid solution $\text{Na}(\text{Gd/La})(\text{MoO}_4)_2$: $\text{Yb}^{3+}/\text{Er}^{3+}$ upconversion nanocrystals with simultaneously enhanced photothermal conversion efficiency and luminescence intensity. *J. Lumin.* **239**, 118356 (2021).
- Teymouri, E., Alemi, A., Aghdam sharabiyani, M. A., Sadeghi, L. & Necefoglu, H. Synthesizes and characterization of new double tungstate $\text{NaRE}(\text{WO}_4)_2$ (RE = Pr^{3+} , Ho^{3+} , Sm^{3+}). *Mater. Chem. Phys.* **240**, 122173 (2020).
- Wang, H. Y. et al. Synthesis of ultrastable copper sulfide nanoclusters via trapping the reaction intermediate: potential anticancer and antibacterial applications. *ACS Appl. Mater. Interfaces.* **7**, 7082–7092 (2015).

37. Toby, B. H. & Von Dreele, R. B. GSAS-II: the genesis of a modern open-source all purpose crystallography software package. *J. Appl. Cryst.* **46**, 544–549 (2013).
38. Marques, V. S. et al. Effect of different solvent ratios (water/ethylene glycol) on the growth process of CaMoO_4 crystals and their optical properties. *Cryst. Growth Des.* **10**, 4752–4768 (2010).
39. Roduner, E. Size matters: why nanomaterials are different. *Chem. Soc. Rev.* **35**, 583–592 (2006).
40. Pandey, A. et al. Photon and electron beam pumped luminescence of Ho^{3+} activated CaMoO_4 phosphor. *Appl. Surf. Sci.* **423**, 1169–1175 (2017).
41. Suresh, B. et al. Amplification of green emission of Ho^{3+} ions in lead silicate glasses by sensitizing with Bi^{3+} ions. *J. Alloys Compd.* **683**, 114–122 (2016).
42. Taniguchi, M. M., Marconi, J. D., Herculano, L. S. & Belançon, M. P. On the prospects of enhance glass based devices with silver nanoparticles: the case of Pr^{3+} doped tellurite-tungstate glasses. *J. Alloys Compd.* **749**, 871–877 (2018).
43. Stojadinović, S. & Ćirić, A. Highly-increased photoluminescence of Pr^{3+} due to the $\text{Eu}^{2+} \rightarrow \text{Pr}^{3+}$ energy transfer in Al_2O_3 coatings formed by plasma electrolytic oxidation. *J. Lumin.* **226**, 117407 (2020).
44. Krishna, R. H. et al. Effect of calcination temperature on structural, photoluminescence, and thermoluminescence properties of $\text{Y}_2\text{O}_3:\text{Eu}^{3+}$ nanophosphor. *J. Phys. Chem. C.* **117**, 1915–1924 (2013).
45. Boyer, J. C., van Veggel, F. C. & J. M. Absolute quantum yield measurements of colloidal $\text{NaYF}_4:\text{Er}^{3+}$, Yb^{3+} upconverting nanoparticles. *Nanoscale* **2**, 1417–1419 (2010).
46. Sundarakannan, B. & Kottaisamy, M. $\text{ZnO}:\text{Al}$ —A yellowish orange emitting phosphor for blue light -converted white light emitting diode (WLEDs). *Ceram. Int.* **44**, 14518–14522 (2018).
47. Laguna, M. et al. Multifunctional Eu -doped $\text{NaGd}(\text{MoO}_4)_2$ nanoparticles functionalized with poly(L-lysine) for optical and MRI imaging. *Dalton Trans.* **45**, 16354–16365 (2016).

Acknowledgements

MC and VRH thank University Grants Commission, India for the NFOBC fellowship and the start-up grant under Faculty Recharge Programme, respectively. DJ and VT kindly acknowledge IIT Gandhinagar for the molecular biology lab facilities. DKD acknowledges PMRF for funding. Research facilities under the University Laboratory for Materials Characterization, Goa University are gratefully acknowledged. The authors thank the financial support from the Department of Science and Technology, New Delhi (PURSE; SR/PURSE/2023/198).

Author contributions

MBC performed synthesis, characterization, visualization and formal analysis of samples. DJ and VT carried out biological studies. DKS and JK performed lifetime measurements. VRH conceptualized the project. The manuscript was written through the contributions of all authors who have approved the final version of the manuscript.

Declarations

Competing interests

The authors declare no competing interests.

Additional information

Supplementary Information The online version contains supplementary material available at <https://doi.org/10.1038/s41598-025-93239-3>.

Correspondence and requests for materials should be addressed to V.R.H.

Reprints and permissions information is available at www.nature.com/reprints.

Publisher's note Springer Nature remains neutral with regard to jurisdictional claims in published maps and institutional affiliations.

Open Access This article is licensed under a Creative Commons Attribution-NonCommercial-NoDerivatives 4.0 International License, which permits any non-commercial use, sharing, distribution and reproduction in any medium or format, as long as you give appropriate credit to the original author(s) and the source, provide a link to the Creative Commons licence, and indicate if you modified the licensed material. You do not have permission under this licence to share adapted material derived from this article or parts of it. The images or other third party material in this article are included in the article's Creative Commons licence, unless indicated otherwise in a credit line to the material. If material is not included in the article's Creative Commons licence and your intended use is not permitted by statutory regulation or exceeds the permitted use, you will need to obtain permission directly from the copyright holder. To view a copy of this licence, visit <http://creativecommons.org/licenses/by-nc-nd/4.0/>.

© The Author(s) 2025